*J. Fluid Mech.* (2012), *vol.* 696, *pp.* 67–93.  
doi:10.1017/jfm.2012.8

# Turbulent mixing in a Richtmyer–Meshkov fluid layer after reshock: velocity and density statistics

**B. J. Balakumar†, G. C. Orlicz, J. R. Ristorcelli, S. Balasubramanian, K. P. Prestridge and C. D. Tomkins**

Physics Division, Los Alamos National Laboratory, Los Alamos, NM 87545, USA

(Received 21 March 2011; revised 29 August 2011; accepted 3 January 2012; first published online 7 March 2012)

The properties of turbulent mixing in a Richtmyer–Meshkov (RM) unstable fluid layer are studied under the impact of a single shock followed by a reshock wave using simultaneous velocity–density measurements to provide new insights into the physics of RM mixing. The experiments were conducted on a varicose $SF_6$ fluid layer (heavy fluid) interposed in air (light fluid) inside a horizontal shock tube at an incident Mach number of 1.21 and a reflected reshock Mach number of 1.14. The light–heavy–light fluid layer is observed to develop a nonlinear growth pattern, with no transition to turbulence upon impact by a single shock (up to $tU/\lambda = 23.4$). However, upon reshock, enhanced mixing between the heavy and light fluids along with a transition to a turbulent state characterized by the generation of significant turbulent velocity fluctuations ($\sigma_u/U \sim 0.3$) is observed. The streamwise and spanwise root-mean-squared velocity fluctuation statistics show similar trends across the fluid layer after reshock, with no observable preference for the direction of the shock wave motion. The measured streamwise mass flux ($\overline{\rho' u'}$) shows opposing signs on either side of the density peak within the fluid layer, consistent with the turbulent material transport being driven along the direction of the density gradient. Measurements of three of the six independent components of the general Reynolds stress tensor ($R_{ij} = \overline{\rho u_i'' u_j''}$) show that the self-correlation terms $R_{11}$ and $R_{22}$ are similar in magnitude across much of the fluid layer, and much larger than the cross-correlation term $R_{12}$. Most importantly, the Reynolds stresses ($R_{ij}$) are dominated by the mean density, cross-velocity product term ($\overline{\rho}\,\overline{u_i' u_j'}$), with the mass flux product and triple correlation terms being negligibly smaller in comparison. A lack of homogeneous mixing (and, possibly, a long-term imprint of the initial conditions) is observed in the spanwise turbulent mass flux measurements, with important implications for the simulation and modelling of RM mixing flows.

**Key words:** nonlinear instability, shock waves, turbulent mixing

## 1. Introduction

Richtmyer–Meshkov (RM) instability refers to the growth of perturbations at an impulsively accelerated interface between two fluids of differing densities driven by the deposition of baroclinic vorticity. The perturbation amplitude grows linearly

† Email address for correspondence: bbalasub@gmail.com

with time during the early phase under certain conditions (Richtmyer 1960; Latini, Schilling & Don 2007; Nishihara *et al.* 2010). When these conditions are not met, the amplitudes exhibit nonlinear growth and, given sufficient initial energy, the flow eventually transitions to a turbulent mixing state. In all these regimes, the net effect of the RM instability is to enhance the mixing between fluids of different densities, which has important consequences for real-life problems. For example, in inertial confinement fusion reactions, the mixing induced by the RM instability (created by surface non-uniformities at the fuel–shell interface or by non-uniform radiation drive) results in the contamination of the fuel and limits the fusion energy gain (Aglitskiy *et al.* 2010). On the contrary, RM instabilities enhance mixing between the oxidizer and the fuel in supersonic engines to improve combustion efficiency (Yang, Kubota & Zukoski 1993). The pearl-necklace patterns observed in supernova explosions and the ejection of heavy elements from supernovae have also been attributed to RM instability (Arnett *et al.* 1987).

A substantial amount of experimental effort has been invested in RM instability studies focused on the initial, linear and early nonlinear periods of RM instability growth, despite the fact that most applications involve high Reynolds numbers and sufficiently large time scales and/or initial energies for the flow to transition to a turbulent mixing regime (Ryutov *et al.* 1999; Robey *et al.* 2003). In these cases, the efficacy of species mixing is heavily influenced by the dynamics of the turbulence contained within the flow. Thus, the development of predictive capabilities for the aforementioned applications requires the accurate measurement and modelling of RM turbulence, especially considering the fact that the dynamics of mixing are not fully understood as yet. For example, the observed mixing transition Reynolds number of turbulence (Robey *et al.* 2003; Dimotakis 2005) and the challenges associated with the development of a wide spectral range in variable-density flows (Cook, Cabot & Miller 2004) have only recently been explained by the theoretical analysis presented in Abarzhi (2010), where it was found that unsteady turbulent mixing exhibits more order and is more sensitive to the initial conditions than canonical turbulence.

The dynamics of variable-density RM turbulence (and mixing) is interesting as it is dependent not only on the velocity field, as in passive scalar mixing, but also on the density fields. Unlike constant-density flows, the density fields in variable-density flows actively modulate the response of the fluids to a given stress condition, and are called level-two mixing flows by Dimotakis (2005). Recent studies have also suggested that the physics of variable-density turbulent mixing might deviate significantly from those of Boussinesq fluids (Ristorcelli & Clark 2004; Livescu & Ristorcelli 2007, 2008; Livescu *et al.* 2009). While numerous experiments involving passive scalar mixing have been performed in the past (see Warhaft 2000, for a recent review), detailed experiments on level-two mixing flows are few in number, despite the possibility of attaining higher Reynolds numbers beyond the reach of direct numerical simulation (DNS) (Cook *et al.* 2004). In this work, we adopt a broad definition of turbulence as an irregular state of flow in which physical quantities possess a cascade and allow the calculation of distinct average values (von Kármán 1938; Hinze 1959). Such a view is necessary to create reasonable models of turbulence in unsteady flows such as RM flows (Besnard *et al.* 1992), and has been widely adopted in several contexts of variable-density turbulence (Chassaing *et al.* 2002; Hill, Pantano & Pullin 2006; Livescu & Ristorcelli 2008). Further, we will follow the metrics and formulation given in Besnard *et al.* (1992), consistent with recent research trends (see e.g. Livescu & Ristorcelli 2007, 2008; Banerjee, Gore & Andrews 2010*a*).

Given the experimental focus in this paper, it is helpful to understand the nature of the difficulties associated with the experimental measurement of variable-density RM mixing flows. RM experiments typically occur within short time scales and require a careful experimental set-up and diagnostic timing. For example, in fluid layers, such as those used at the Los Alamos National Laboratory's gas shock tube facility, even at low Mach numbers ($Ma = 1.2$), strong mixing occurs within the first 2–3 ms of the first shock impact. This event duration is further reduced in the presence of multiple shocks, as evidenced by the enhanced mixing observed within the first 100 μs of a reshock impact (Balakumar *et al.* 2008). Therefore, the accumulation of large sets of statistics requires either high-frequency data acquisition diagnostics (for time averaging) or highly repeatable experimental runs with short turnaround times (for true ensemble measurements). RM flows also involve strong spatial gradients and vortex fields, the capture of which requires high-resolution diagnostics. The computation of reliable ensemble statistics requires a repeatable initial condition that does not change the base flow upon which the turbulent flow field is superimposed. Thus, the challenges of measuring density and velocity fields simultaneously, in multiple realizations of the same experiments, with adequate spatial resolution, on stable initial conditions, have combined to slow down progress in the experimental study of RM turbulence.

The diagnostics deployed on RM mixing flows thus far suffer from the major limitation of an inability to perform simultaneous density–velocity measurements at multiple points in the flow fields. Previous work on RM turbulence has been confined to the use of simple optical (Schlieren, shadowgraphy), thermal anemometry or laser Doppler anemometry (LDA) diagnostics that provide only limited information about the flow. Such optical techniques, while easy to implement, are limited to the measurement of gross metrics, such as mixing zone width and growth rate measurements of the mixing zone, owing to resolution limitations imposed by beam path averaging. Further, the interrogation beams for Schlieren and shadowgraphy pass through the wall boundary layers of the shock tube, introducing large errors in the reported width measurements (Jacobs *et al.* 1995). Recently, the use of holographic velocimetry for three-dimensional velocity measurements in variable-density flows has been proposed (Orlov *et al.* 2010). Thermal anemometry offers high data rates but is limited by its intrusive nature. Recent efforts in the use of hot wires to measure density and velocity have proven to be considerably challenging (Mariani *et al.* 2009; Banerjee, Kraft & Andrews 2010*b*). Thermal anemometry is also incapable of measuring statistics at multiple points within the flow field without intrusion, especially in the presence of shock waves. Finally, calibration of thermal anemometers in variable-density flows with thermal variations (as in RM turbulence) is a non-trivial task, relegating thermal anemometry to the measurement of only shock widths in RM flows (Jourdan *et al.* 2001). LDA diagnostics have been used with greater success in RM flows. For example, Poggi, Thorembey & Rodriguez (1998) have measured the velocity fluctuations inside a turbulent mixing zone induced by shock interaction(s) with a single interface using a high-sampling-rate LDA burst sampler. As they have noted, LDA measurements yield only single-point turbulent velocity statistics and require the generation of an ensemble of RM mixing data to calculate velocity variances. Moreover, in RM mixing, both density and velocity fluctuations are important and should be measured at the same instant of time in order to calculate the true Reynolds stresses. These limitations can now be overcome with simultaneous, high-resolution, particle image velocimetry–planar laser-induced

fluorescence (PIV–PLIF) diagnostics, which have been developed and applied to RM mixing flows recently (Balakumar *et al.* 2008).

Simultaneous PIV–PLIF diagnostics provide the instantaneous velocity and density fields inside turbulent flows at multiple points and are minimally intrusive. In the present work, a two-dimensional PIV diagnostic, in conjunction with an acetone–PLIF diagnostic, is used to measure simultaneously the evolution of velocity and density fields in a gas curtain before and after reshock. Statistics are measured from an ensemble generated from several runs of the same experiment. Each run was started from closely controlled initial conditions and shock wave parameters to measure mean and turbulence velocity and density statistics, mixing parameters such as the density self-correlation parameter, mass flux and Favre-averaged Reynolds stresses. The present work involves the most detailed measurements in RM flows thus far and measures hitherto unknown turbulence quantities for the first time in RM flows. In addition to providing new experimental insights into variable-density turbulent mixing, the present data also enable a detailed comparison of experimentally measured turbulence statistics to the predictions of numerical simulations (Hill *et al.* 2006; Gowardhan, Grinstein & Wachtor 2010; Thornber *et al.* 2010). Some simulations using implicit large-eddy simulation techniques have been performed on the experimental configurations presented here, although the comparisons have been limited to only a few turbulence variables thus far (Zoldi-Sood *et al.* 2008; Gowardhan & Grinstein 2010; Gowardhan *et al.* 2011).

## 2. Experimental details

### 2.1. *Shock tube apparatus and diagnostics*

The experiments reported here were performed in a 75 mm square diaphragm-driven horizontal shock tube facility at Los Alamos National Laboratory. The first shock (Mach 1.21) is created by the rupture of a polypropylene diaphragm that separates the high-pressure driver gas (nitrogen) from ambient air inside the shock tube. The shock wave travels down the shock tube to impinge upon the initial conditions consisting of a thin fluid layer of $SF_6$ interposed across the test section to generate the RM instability. Subsequently, the transmitted shock that has passed through the curtain travels down the tube and is reflected by a rigid wall located 0.137 m downstream of the initial conditions. The reflected shock (Mach 1.14) impinges once again on the developing fluid layer to deposit additional vorticity. This event is called the reshock, and the reflected shock wave is called the reshock wave.

The RM instability is driven by the baroclinic vorticity deposited due to a misalignment between the density and pressure gradients. Since the shock waves in the present experiments are planar, an initial condition with a corrugated density distribution is required for generating RM instability. In the present experiments, initial conditions consisting of varicose spatial perturbations on a temporally steady heavy gas curtain of $SF_6$ were used to create this density gradient. The thin fluid layer with varicose perturbations is generated by passing $SF_6$ through a suitably profiled nozzle containing a closely spaced array of holes at its exit. Diffusion and convective processes together act to create a layer containing varicose perturbations on either edge. This fluid layer is introduced into the shock tube by locating the nozzle exit at the top wall. The $SF_6$ flows through the cross-section of the shock tube by gravity and is removed by a suction manifold attached to the bottom wall of the horizontal shock tube. One prominent difference between the present series of experiments and previous experiments is the stability of the initial condition. Gas curtains flowing in enclosed

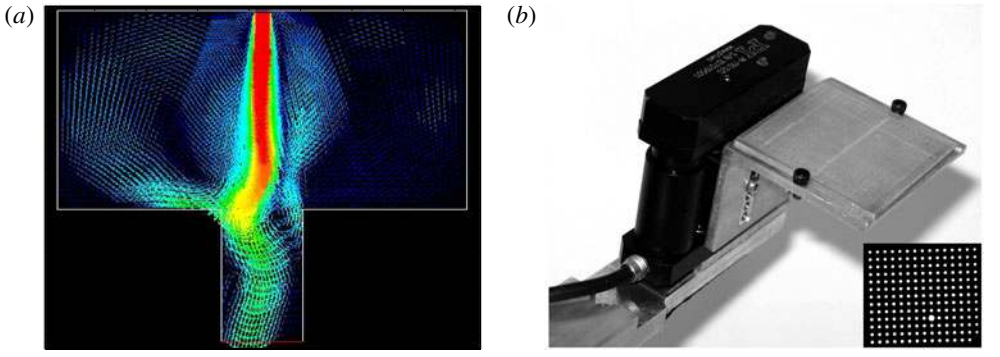


FIGURE 1. (*a*) Instantaneous snapshot from a time-resolved laminar flow simulation illustrating the oscillating instability of a confined gas jet. This instability is mitigated in the present experiments by using a passive air–$SF_6$–air co-flow configuration. Vectors represent velocity and colours represent magnitude of velocity, with red and blue representing high and low velocities, respectively. (*b*) Calibration apparatus used to calculate third-order polynomial functions for superimposing velocity and density fields, shown along with a sample calibration image (inset).

environments have been known to be unstable (Maurel *et al.* 1996). The interactions of the shear-driven vortices on either side of the layer with the vortex created near the suction manifold cause an unstable flapping of the curtain, which disturbs the steady state of the initial conditions (figure 1*a*). This instability was mitigated in the present experiments by deploying two openings on either side of the nozzle. These openings created a co-flowing curtain of air–$SF_6$–air that reduced the shear at the edges to create a very stable curtain yielding repeatable initial conditions that were used to obtain the statistics presented here.

During each run of the experiment, a Mach 1.21 shock impinges upon the fluid layer to deposit baroclinic vorticity. The evolving interfaces are then subjected (after $t = 600$ μs) to a second interaction with a reflected reshock wave (Mach 1.14) that deposits additional energy and induces a transition to a turbulent state. A reshock wave is employed in the present experiments to induce a rapid transition to turbulence (relative to the duration of shock propagation across the shock tube). This allows the study of turbulent RM mixing in isolation from the impact of additional reflected rarefaction and compression waves that are typically present in a shock tube apparatus. Secondly, a reshock wave is representative of what happens in applications (e.g. inertial confinement fusion), where multiple shock interactions are common. Thirdly, in the flows investigated here, it has been observed earlier that coherent initial perturbations in the flow dynamics remain ordered in a single-shock system until late times (Balakumar *et al.* 2008). A reshock wave induces the dissociation of this order and the generation of smaller scales (akin to a cascade). Finally, a two-shock system (in contrast to a multi-shock system) is the simplest configuration that deviates from a single-shock system, and was therefore used in the present experiments. Also, the present experimental apparatus does not allow for more than two shocks to be generated in a single run of the experiments.

The turbulent RM mixing structure generated in the shock tube is studied using planar, simultaneous PIV–PLIF diagnostics to obtain instantaneous velocity–density statistics. Turbulence statistics are calculated as ensemble averages, followed by spanwise averages in the periodic direction where applicable. All of the turbulence

data presented in this paper were obtained at $t = 800$ μs after first shock corresponding to $t = 200$ μs after reshock. These correspond to non-dimensional times ($t^* = tU/\lambda$) of 22.9 and 5.7, respectively. Here, $U$ denotes the particle velocity behind the first shock (103.3 m s$^{-1}$), $t$ represents the absolute time elapsed since the impingement of the first shock upon the initial condition and $\lambda$ represents the primary wavelength of the initial condition (3.6 mm). The reshock time was adjusted by fixing the end wall location at an appropriate distance from the initial conditions. The reshock time was selected to occur when the initial perturbations on the curtain had grown sufficiently convoluted to represent several zero crossings of the density gradient along the centreline (Balasubramanian *et al.* 2011). Under these conditions, the reshock wave has been shown to be most effective in driving the fluid layer to a state of turbulent mixing (Balasubramanian *et al.* 2011).

During each run of the experiment, two instantaneous PLIF and a pair of PIV images are captured. The heavy gas ($SF_6$) is seeded with acetone vapour and fog droplets prior to entry into the shock tube. The evolving instability is interrogated by two pulses each from a 266 nm and a 532 nm dual-head Nd:YAG pulsed laser. The laser beams are shaped into thin laser sheets of thickness less than 0.5 mm (as measured using marking paper). The PLIF images are captured by a pair of Apogee cameras and the PIV images are captured by a Kodak Megaplus 2k × 2k cross-correlation camera. The PLIF and PIV cameras are equipped with suitable visible-light interference filters and Raman notch filters to eliminate spurious signals from the PIV and PLIF lasers, respectively. One of the PLIF images is always obtained at $t = 515$ μs ($t^* = 14.8$) after first shock to act as a reference image. Any changes in the reference image from the nominal caused by a modification of the initial condition or experimental conditions are thus detected during every run of the experiment. Data from such deviant runs of the experiment are discarded during the calculation of the statistics presented here. The PLIF resolution of the evolving curtain is 51.8 μm pixel$^{-1}$, while the vector-to-vector spacing for the PIV fields is 181 μm, corresponding to a pixel resolution of 15.1 μm pixel$^{-1}$ on the PIV camera.

It is critical to calibrate the PIV and PLIF cameras accurately in order to superimpose the density and velocity fields spatially. Previous experience shows that simple calibration procedures using fixed rulers are prone to errors and result in significant spatial offsets and magnification variations across the density and velocity fields. Therefore, a plate with an array of accurately positioned through-holes mounted on a high-accuracy translation stage ($\leqslant$50 nm accuracy) was used to perform the calibrations by back-lighting the holes (figure 1*b*). Covering the holes with translucent tape and carefully positioning the light sources allowed the precise determination of the hole centres on the image plane using a centroid identification procedure. The spatial locations of the holes on the image planes were then mapped to the spatial location of the holes in the measurement space using a third-order polynomial mapping function following the procedure detailed in Soloff, Adrian & Liu (1997). To compensate for the location of the PIV and PLIF cameras on either side of the calibration target, the target was moved to place the imaged end of the holes at the same spatial locations for all cameras. Further details about the experimental apparatus and characterization of the initial conditions are provided in Balakumar *et al.* (2008). All initial condition parameters in the present experiments are identical to those presented in Balakumar *et al.* (2008) except for the peak concentration (Atwood number, $At = 0.6$ in our present experiments).

### 2.2. *Shot-to-shot variations*

Unlike some classes of canonical turbulent flows in the laboratory (such as channel flows, pipe flows and flat-plate zero-pressure-gradient boundary layers), whose statistics are generally considered to be insensitive to minor variations in the initial conditions, the sensitivity of the RM turbulence statistics to small changes in initial conditions is currently unclear – see Ristorcelli & Clark (2004), Livescu & Ristorcelli (2007, 2008), Livescu *et al.* (2009) and Abarzhi (2010) for discussions on the sensitivity properties of variable-density turbulence. Hence, turbulence statistics for RM flows must be calculated from carefully controlled initial conditions. The ensemble averages in the present experiments are created by assembling instantaneous realizations from several runs of the same experiment, and variations between the runs can introduce spurious increases in the calculated turbulence intensities. Therefore, it is important to measure and document the variations between the individual realizations in the present experiments, and it is expected that this additional step in characterizing the experiments will help to answer future questions that arise during comparisons with numerical simulations.

The density measurements obtained using the fluorescence signals induced by the 266 nm pulsed Nd:YAG laser are subject to errors due to laser intensity variations between shots. Since the density calibrations are performed independently of the instantaneous measurements (either before or after the experimental runs), variations of the laser intensity between shots directly translate to fluctuations in the density field. Note that, unlike true turbulence density fluctuations, these fluctuations are correlated within the same realization, and can be removed systematically from the PLIF measurements by measuring the laser pulse intensities. The net laser intensity for each measurement pulse during each run of the experiment was measured by deflecting a portion of the laser beam into a photo-sensor and recording it digitally. Based on 100 measurements, it was found that the instantaneous laser energy varied by less than 3.5 % of the mean energy.

Another source of error in the measurement of turbulence statistics arises from the variation of the shock speed between shots. Shock speed variations manifest themselves in two different ways in the measurement of the statistics: (*a*) changes in the initial baroclinic vorticity deposition due to shock strength variations; and (*b*) variation in the location of the turbulent structure between shots. The first error was found to be negligible, while the second source of error is significant and requires a careful selection of a subset of realizations from all the experimental runs to calculate ensemble statistics. The measured variation of the shock speed (based on pressure transducers located along the wall of the shock tube) was about $\pm 0.5$ %. This translates to an equivalent percentage error in the circulation and is negligible. However, the same variation in the shock speed also translates to a particle velocity variation of about $\pm 2$ m s$^{-1}$, resulting in a jitter in the instantaneous location of the turbulent structure of about $\pm 2$ mm. Since the structure width after reshock is 5.2 mm, this jitter in the instantaneous location is significant when instantaneous fields are superimposed to calculate single-point statistics. That is, superimposing the ensemble of instantaneous realizations without accounting for the shot-to-shot variations in the structure location would contaminate the instantaneous statistics with the streamwise two-point correlation functions (Adrian & Westerweel 2010). While one might consider displacing the measured instantaneous structure prior to calculating the ensemble statistics to compensate for the shock speed variations, we took the stricter approach of utilizing only those realizations in the ensemble whose structures are within 250 μm of one another along the streamwise direction (corresponding to a

pixel displacement of ±5 pixels for the PLIF images). One advantage of this approach is that PIV ensemble averages can be calculated by a direct superposition rather than correcting for the locations, since a ±5 pixel variation in the PLIF images corresponds to a ±16 pixel variation in the PIV images, which is within the vector-to-vector spacing. A more important advantage of this approach is that the timing of the reshock impact between the realizations of the ensemble is preserved, thereby increasing the reliability of the calculated statistics. The Atwood number variation between shots is negligible, since the ambient temperature is maintained constant and ultra-pure gases are used in creating the initial conditions.

### 2.3. *Measurement and statistical error estimates*

#### 2.3.1. *PIV and PLIF measurements*

The PIV image pairs were interrogated using $24 \times 24$ pixel windows and 50 % overlap using the Insight 3G (ver. 9.0.3.2) software. The vector field was validated using standard-deviation filters ($\sigma = 3$) and mildly smoothed using a Gaussian filter ($\sigma = 0.8$ over a $5 \times 5$ vector neighbourhood). Instantaneous velocity vectors were estimated to carry a sub-pixel error of 0.1 pixel corresponding to an absolute error of 0.75 m $s^{-1}$ on the fluctuation fields. Although this error does not propagate into the mean velocity measurements, there is a small (<10 %) bias created on the root-mean-squared (r.m.s.) statistics of the velocity field. This error is less than the statistical convergence error.

The concentration profiles and peak concentration in the initial conditions were characterized using quantitative PLIF measurements. Intensity images of the flowing curtain were obtained before shock impact. These intensities were converted to density measurements using a calibration procedure that employed an anodized nozzle flowing pure (100 %) $SF_6$ (seeded with acetone) and placed above the light sheet. The position of the nozzle was adjusted to preclude errors due to spatial variations of the laser light sheet intensity. The measured PLIF intensity across the nozzle exhibited exponential decay in the direction of the light sheet (Beer's law). Curve fits to the intensity variations in both the spanwise and streamwise directions were used to measure the extinction coefficients. Using these extinction coefficients, the errors due to light absorption on the measured peak intensity were calculated to be less than 1.5 %. The variation in the instantaneous density measurements (without correcting for shot-to-shot laser pulse intensities) was estimated to be 3.5 % and provide a bound for the peak density variation in the initial condition. The laser pulse intensities were also measured using a pyroelectric joulemeter. Corrections for the instantaneous density fields using these measurements resulted in small (<10 %) errors on the density self-correlation profiles that were within the statistical measurement uncertainty. We also note that our measurements are generally presented without normalization. This is because several of the variables presented here are being measured in RM flows for the first time. In these flows, the appropriate scaling variables to use are unclear and remain open problems. Such a method of presentation does not diminish the value of these measurements in providing useful insights into RM turbulence and allows a more stringent validation of simulations.

#### 2.3.2. *Mass conservation estimate*

Since it is non-trivial to calibrate the fluorescent signals from the fluid layer after one or more shocks inside the confined shock tube, the relationship between the concentration of the shocked fluid and the measured PLIF image intensity was established using mass conservation (Tomkins *et al.* 2008). Although mixing might

entrain air, the mass of the fluorescent fluid will remain the same before first shock, after first shock and after reshock. Therefore, by measuring the total mass of the fluorescent fluid in the initial condition before first shock using the aforementioned calibration procedure with a nozzle flowing pure $SF_6$, one can calculate the scaling coefficient ($\alpha$) in the relation $c = \alpha I$ both before and after reshock. Here, $I$ represents the measured charge-coupled device (CCD) pixel count on the PLIF camera and $c$ represents the $SF_6$ concentration. The light sheet was also adjusted such that it maintained the same thickness through the test section. That is, the waist of the light sheet occurred at the midpoint of the measurement stations and minimal variations in the light sheet thickness were measured on either side of the waist near the measurement locations. Using this procedure, the total mass of the heavy gas contained within the control volume was measured to carry a statistical error of $\pm 2\,\%$.

2.3.3. *Uncertainty estimates*

Owing to the difficulties associated with repeating RM experiments from closely controlled initial conditions, RM turbulence statistics must be computed from only a limited number of realizations, introducing sampling errors. The errors associated with the finite sample size used in calculating the turbulence quantities are estimated following the general procedure given in Bevington (1969). The procedure is briefly summarized here for completeness.

Consider an estimate ($\hat{x}$) for a variable, $x$, calculated as

$$\hat{x} = f(U_1, U_2, U_3, \ldots), \tag{2.1}$$

where $U_1, U_2, \ldots$ could be any variable used in the calculation, such as the instantaneous measurement values, actual (error-free) values, or measurement errors. To illustrate the general procedure, let us consider the mean velocity estimate $\widehat{U} = (\sum U_i)/N$, where $U_i$ are the instantaneous measured velocity values. Then, the variance of this estimate is given by (Bevington 1969)

$$\sigma_{\widehat{U}}^2 = \sigma_{U_1}^2 \left(\frac{\partial f}{\partial U_1}\right)^2 + \sigma_{U_2}^2 \left(\frac{\partial f}{\partial U_2}\right)^2 + \cdots + 2\sigma_{U_1U_2} \left(\frac{\partial f}{\partial U_1}\right)\left(\frac{\partial f}{\partial U_2}\right) + 2\sigma_{U_1U_3} \left(\frac{\partial f}{\partial U_1}\right)\left(\frac{\partial f}{\partial U_3}\right) + \cdots, \tag{2.2}$$

where $\sigma_{U_i}^2$ is the variance of the quantity $U_i$ and $\sigma_{U_iU_j}$ is the covariance of the quantities $U_i$ and $U_j$. Estimates of several turbulence quantities calculated in this paper are presented in table 1, assuming independent measurements (i.e. vanishing covariances in (2.2)). More detailed discussions along with different methods of calculating errors in turbulence quantities can be found in Benedict & Gould (1996).

## 3. Results

### 3.1. *Growth of the instability before and after reshock*

The variation of the width of an RM unstable fluid layer with time is often used as a gross metric to characterize the instability growth. Although easy to measure, the effects of refraction of light rays at the wall of the shock tube due to the presence of boundary layers introduce errors that depend upon the diagnostic technique. In particular, Schlieren and shadowgraphy techniques could introduce significant deviations from actual values owing to the volume-averaged nature of the measurement (Jacobs *et al.* 1995). While PLIF measurements are also prone to such errors, PLIF

| Quantity estimated ($\hat{x}$) | Standard deviation of estimate ($\sigma_{\hat{x}}$) | Statistical error, $1\sigma$ (%) |
|---|---|---|
| Mean ($\hat{\rho}$, $\widehat{U}$, $\widehat{V}$, $\widehat{W}$) | $\sqrt{\frac{\sigma_x^2}{N}}$ | $\pm 1$ |
| Variance ($\sigma_\rho^2$, $\sigma_u^2$, $\sigma_v^2$, $\sigma_w^2$) | $2\sqrt{\frac{\sigma_x^4}{N}}$ | $\pm 3$ |
| Density self-correlation ($b$) | $\frac{1}{\sqrt{N}\langle\rho\rangle}\sqrt{\sigma_\rho^2\left[\left\lvert\langle\rho\rangle^4\left\langle\frac{1}{\rho^4}\right\rangle+(1+b)^2-2(1+b)\left\langle\frac{1}{\rho^2}\right\rangle\langle\rho\rangle^2\right\rvert\right]}$ | $\pm 15$ |
| Mass flux ($a_1$, for example) | $\frac{1}{\sqrt{N}}\sqrt{\frac{2\sigma_u^2\sigma_\rho^2+2\sigma_{\rho u}^2}{\hat{\rho}^2}+\frac{\sigma_u^2\sigma_{\rho u}^2}{\hat{\rho}^4}}$ | $\pm 20$ |
| First term in $R_{ij}$ expansion $\overline{\rho}\,\overline{u_i'u_j'}$ | $\frac{1}{\sqrt{N}}\sqrt{\langle uv\rangle^2\sigma_\rho^2+2\langle\rho\rangle^2(\sigma_u^2\sigma_v^2+\sigma_{uv}^4)}$ | $\pm 4$ |

TABLE 1. Statistical and measurement errors associated with the turbulence measurements.

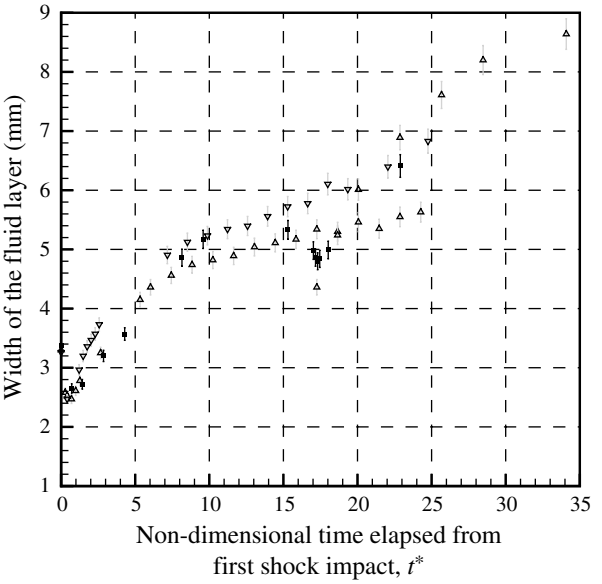


FIGURE 2. Growth of the RM unstable fluid layer after first shock and after reshock in the present experiments (■), compared to previous data from nominally identical initial conditions (△, Balakumar *et al.* 2008; ▽, Orlicz *et al.* 2009).

diagnostics offer quantitative density fields, making them superior to line-of-sight techniques.

The presence of noise in the recorded PLIF images is another salient source of variability in the measured widths. Based on width measurements from several realizations, and after accounting for potential shot-to-shot variations in the illumination intensity (which directly affect the width for a given fixed threshold of pixel intensity), it is estimated that the widths in the present measurements are accurate to within ±3 %.

The variation of the measured layer width with time is shown in figure 2. The widths are measured between locations where the concentration of $SF_6$ falls to 5 %. Data from previous experiments on a varicose initial condition that is nominally identical to the present experiments are also plotted for comparison (Balakumar *et al.* 2008; Orlicz *et al.* 2009). The present data fall within ±5 % of the previously measured widths. It should be noted that these data sets were obtained with two different set-ups on experiments that were conducted several months apart. Despite this, the small variation in the measured widths between these data sets is an immediate indicator of the repeatability of the present experimental set-up. Qualitatively, the structures in the present data were found to be very similar to the structures observed in Balakumar *et al.* (2008), especially during the early growth phase up to 200 μs ($t^* = 5.7$).

The maximum growth rate of the curtain after first shock occurs between $t^* = 2.9$ and 11.4. During this time, the layer width grows at an average rate of 8.7 m s$^{-1}$. Subsequently, the growth of the singly shocked curtain slows down and reduces to a value that is approximately an order of magnitude smaller until reshock. Upon reshock, the growth rate once again increases dramatically to reach a value of 7.6 m s$^{-1}$, at $t^* = 2.9$ after reshock. The corresponding bulk Reynolds number ($Re = h\dot{h}/\nu$, where $h$

is the layer width and $\nu$ is the viscosity of a 50 % $SF_6$–air mixture at ambient conditions) changed from $Re = 691$ before reshock to $Re = 3275$ after reshock.

These detailed measurements of the curtain width and growth rate provide an opportunity to compare the results of numerical simulations with experiments. Our experience in comparing two- and three-dimensional codes with experimental results has shown that matching the growth rates between experiments and simulations is achieved with much less effort than a comparison of absolute widths.

### 3.2. *Transition during reshock*

A time series showing the transition of the RM fluid layer into a strongly mixed state after reshock is presented in figure 3. Rapid material mixing occurs within the first 100 μs of reshock (corresponding to a duration of $t^* = 2.9$). During this time ($17.2 \leqslant t^* \leqslant 20.0$), vortical structures are observed in the fluid layer at $t^* = 18.0$ and $t^* = 18.9$. The large-scale symmetry present before reshock is destroyed to create small-scale vortical structures, some of which are not symmetric (as is clear from the upstream structures at $t^* = 18.9$). The presence of these vortical structures is interesting, as it allows for the possibility of modelling RM turbulence after reshock using elementary vortex dynamics similar to the wall-turbulence models proposed in the past (Marusic 2001). It is worthwhile noting that the baroclinic vorticity deposition mechanism is active during both the first shock passage and the reshock (see also Velikovich *et al.* 2000; Nishihara *et al.* 2010). In the case of reshock, however, the convoluted interface (i.e. density gradients) present just prior to reshock results in a more complex deposited vorticity field, and thus faster transition to a state of turbulent mixing. This might offer a clue in the choice of metrics to determine transition. Note that the dynamics of the flow, driven by vortical interactions, among other mechanisms, is complex and is not fully understood as yet. The focus of the present paper is the statistics of the turbulent (or near-turbulent) state, so our discussion of the transition process here is limited. Further discussion about the fine-scale structure of the fluid layer in this early turbulent state is provided elsewhere, however, including before and after reshock (Balakumar *et al.* 2008) for $M = 1.2$ and prior to reshock (Orlicz *et al.* 2009) for $M = 1.2$ and 1.5. Note that the turbulence statistics presented in the present paper are obtained well past this transition, at $t^* = 22.9$.

There is one aspect of the post-reshock transition that may be illuminated by the present data, and so will be discussed here. The enhanced mixing after reshock may be understood by looking at the PIV–PLIF fields of the evolving curtain immediately after reshock. Figure 4 shows that the post-reshock mixing is driven by four large-scale vortices, presumably created by the roll-up of baroclinic vortex sheets deposited at the material interfaces. Unlike the pre-reshock case, which is driven by a row of approximately equispaced counter-rotating vortices, the post-reshock flow is driven by two rows of counter-rotating vortices arranged as shown in figure 4. This latter arrangement is unstable, and therefore small perturbations after reshock would result in the dislocation of the vortices. Thus, in the post-reshock case, mixing is probably driven both by vortex-induced fluid motion *and* by the motion of the vortices themselves, resulting in a faster transition to a turbulent state when compared to the singly shocked case.

### 3.3. *First shock and reshock wave properties*

The propagation velocities of the first shock and reshock waves were independently measured in the present experiments using pressure transducers installed in the walls of the shock tube. Based on these data, the incident shock Mach number was

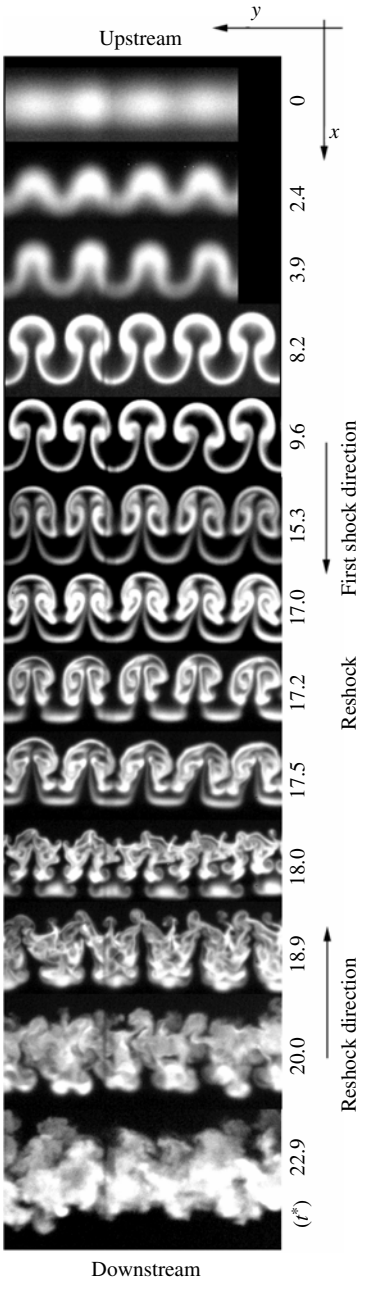


FIGURE 3. Time-series PLIF images showing transition of the RM unstable fluid layer after reshock at $t = 600$ μs ($t^* = 17.2$).

calculated to be 1.21. One-dimensional gas dynamics calculations, after accounting for the transmission and reflection of the shock wave through a perturbation-free air–$SF_6$–air interface, yielded a reflected shock Mach number of 1.14. In a non-porous wall, the particle velocity behind the reshock wave is expected to be zero. However, we observe a non-zero velocity behind the reshock wave, potentially due to leakages

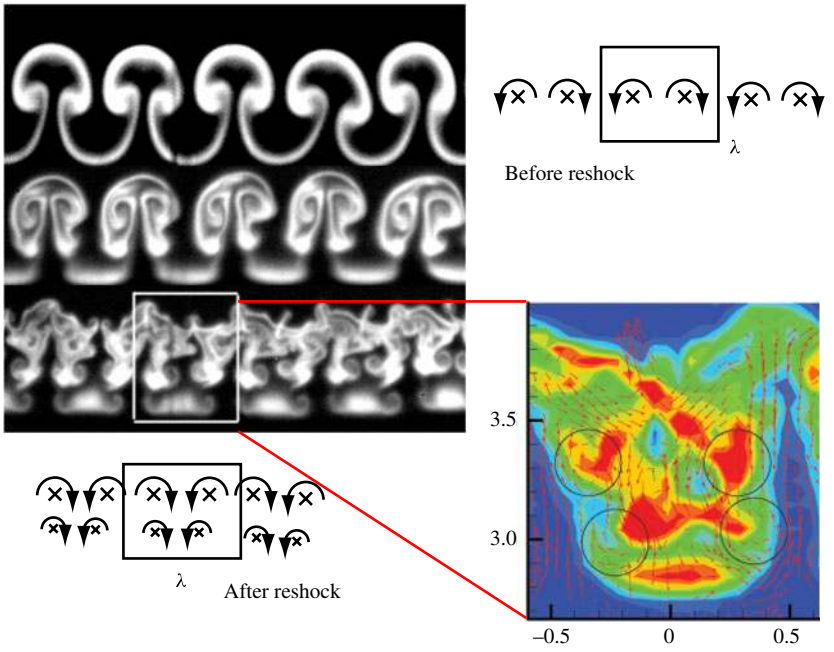


FIGURE 4. Simultaneous PIV–PLIF field showing multiple interacting vortices immediately after reshock.

around the reshock wall. It should be noted that the incident shock wave incurs losses during its reflection from the fluid layer interfaces and due to the suction manifold. Shock wave distortions also occur upon its passage through the convoluted light–heavy–light fluid layer interface. In the present experiments, the value of the reflected shock speed was verified to be consistent with pressure trace measurements from pressure transducers to within $\pm 10\,\%$. The ambient pressure in the shock tube is measured to be 78 kPa and must be accounted for in numerical simulations.

### 3.4. *Mean propagation velocity of the fluid layer's centre of mass*

The mean propagation velocity of the fluid layer is strongly dependent upon the distribution of the baroclinic vorticity in the layer after its interactions with the shock wave. In a flat fluid layer with no perturbations, the first shock impacting the initial condition accelerates the curtain to the particle velocity of the transmitted shock and no baroclinic vorticity is generated. However, the presence of baroclinic vorticity in a corrugated fluid layer modifies the translation velocity of the fluid layer and may cause a deviation from the particle velocity of the shock due to self-induction. Thus, accurately capturing the centre-of-mass variation with time is one indicator of the ability of a simulation to capture the baroclinic vorticity deposition accurately.

Displacement of the centre of mass of the fluid layer at various times after the shock wave, calculated from the density fields measured from the PLIF diagnostic, is shown in figure 5. Linear curve fits to the centre-of-mass location yielded mean translation velocities of 103.3 and 30.0 m $s^{-1}$ before and after reshock, respectively. The post-reshock velocity of the fluid layer does not reduce to zero because the interface and the transmitted shock are perturbed.

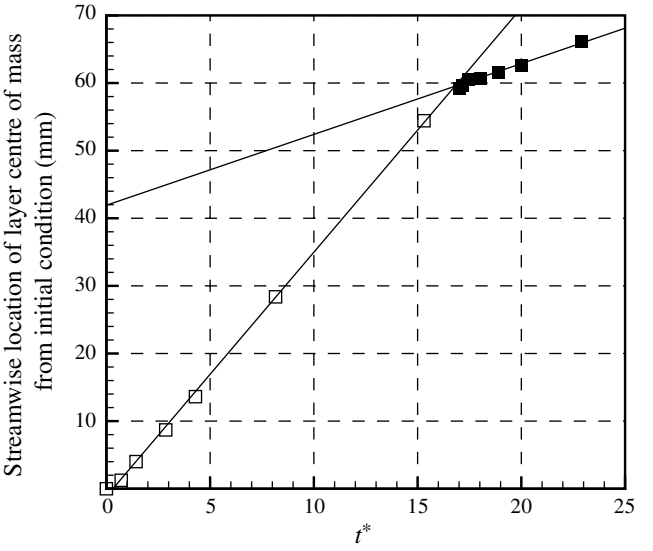


FIGURE 5. Displacement of the centre of mass of fluid layer with time. The lines represent linear curve fits to the data and yield a mean convection velocity of 103.3 m s$^{-1}$ before reshock (□) and 30.9 m s$^{-1}$ after reshock (■).

### 3.5. *Ensemble-averaged mean velocity statistics*

The instantaneous velocity fields that drive the mixing were directly measured using PIV. The mean streamwise and wall-normal velocity variations of the reshocked structure in the streamwise direction at $t^* = 22.9$ are shown in figure 6(*a*). The mean velocities were calculated as the spanwise average of the ensemble-averaged velocity fields. The spanwise mean velocity approaches zero, as is expected from the symmetry of the initial conditions. The mean streamwise velocity varies between 25 and 30 m s$^{-1}$ across the layer, with the downstream edge (with respect to the direction of the first shock) moving faster than the upstream edge. This variation is consistent with a reshocked structure that is increasing in width over time.

Figure 6(*b*) plots the area histograms of the instantaneous spanwise and streamwise velocities along with their least-squares Gaussian fits. The histograms are generated using the velocity fields from all nine of the valid instantaneous PIV realizations. Both the spanwise and streamwise velocities show approximately symmetric distributions about their mean values (−0.31 and 27.2 m s$^{-1}$, respectively). Based on the Gaussian fits, the streamwise velocity shows a slightly larger standard deviation (10.1 m s$^{-1}$) in comparison to the spanwise velocity (8.2 m s$^{-1}$). In both cases, the velocity fluctuations are significant in comparison to the mean velocity and are larger than the previously measured values at an earlier time (Balakumar *et al.* 2008), indicating turbulence production long after the shock wave has passed through the fluid layer, presumably due to variable-density turbulence effects. It should be noted that the histograms and velocity statistics presented in this paper are derived from seeding only the heavy gas, owing to difficulties associated with seeding the surrounding light gas. The measurement bias introduced by this selective seeding is not expected to be significant at the present measurement time because of the strongly mixed state of the fluid layer after reshock.

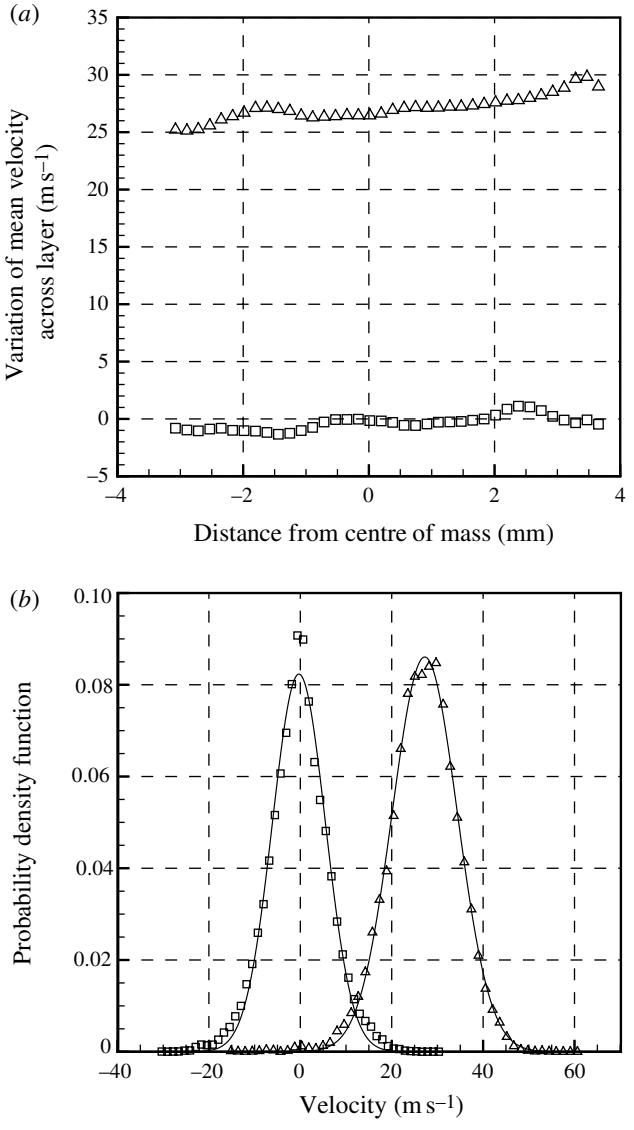


FIGURE 6. (*a*) Variation of the mean streamwise (△) and spanwise (□) velocity across the fluid layer after reshock ($t^* = 22.9$). (*b*) Area histograms of the instantaneous streamwise (△) and spanwise (□) velocities within the fluid layer ($t^* = 22.9$).

### 3.6. *Turbulence statistics: velocity fluctuations*

The streamwise and spanwise velocity variances across the fluid layer after reshock ($t^* = 22.9$) are plotted in figure 7(*a*). These variances are calculated as the spanwise averages of ensemble statistics. It is clear that the streamwise and spanwise velocity variances are approximately equal in magnitude throughout the fluid layer (within statistical convergence errors), indicating that any anisotropy in the velocity field along the direction of shock propagation is less than the statistical measurement errors. The r.m.s. streamwise velocity fluctuation reaches a peak value of 30 % of the mean velocity at the centreline and reduces to ∼20 % on either edge of the fluid layer.

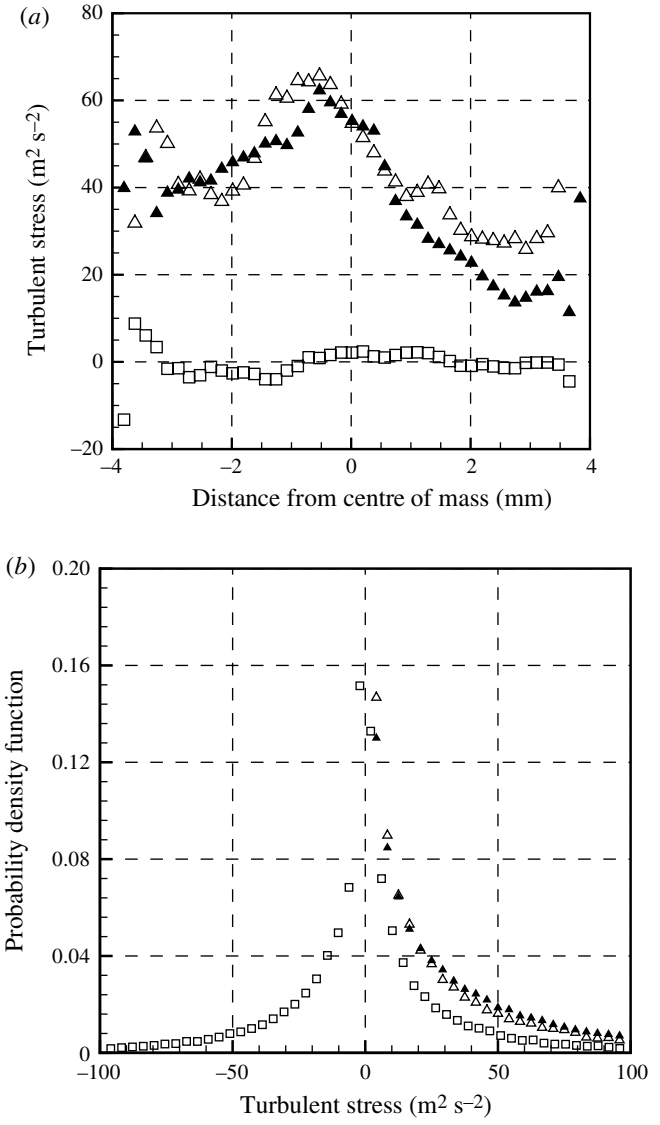


FIGURE 7. (*a*) Variances of the velocity fluctuations across the fluid layer at $t^* = 22.9$. (*b*) Area histograms of $\overline{u_1'^2}$, $\overline{u_2'^2}$ and $\overline{u_1'u_2'}$ statistics at the same time. For both panels: △, $\overline{u_1'^2}$; ▲, $\overline{u_2'^2}$; □, $\overline{u_1'u_2'}$.

The cross-correlation component ($\overline{u_1'u_2'}$, where 1 and 2 represent the streamwise and spanwise directions, respectively), related to the generalized Reynolds shear stress, is smaller than the streamwise and spanwise velocity variances by more than an order of magnitude throughout the fluid layer. This behaviour is typical of a well-mixed fluid layer that is homogeneous in the spanwise direction, since a given streamwise velocity fluctuation is equally likely to produce a spanwise fluctuation in either direction. However, the spanwise average of $\langle u_1'u_2' \rangle$ will also vanish for a fluid layer that is reflectionally symmetric (but not homogeneous) in the spanwise direction, since equal and opposite signs of correlations occur on either side of the axis of symmetry. Since

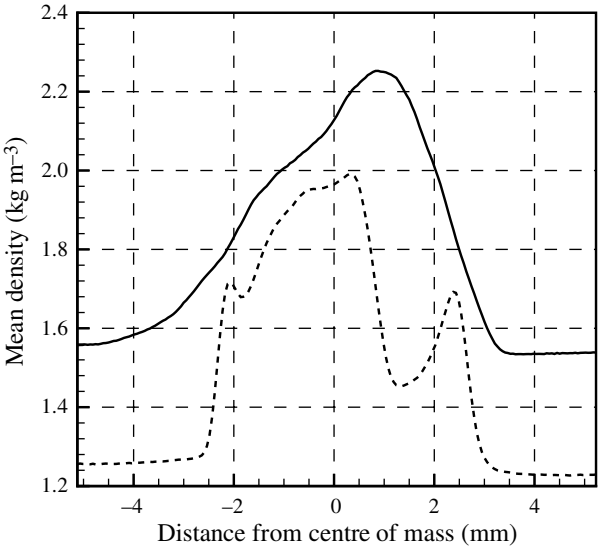


FIGURE 8. Mean density variation across the fluid layer before ($t^* = 15.4$; – – –) and after reshock ($t^* = 22.9$; ———).

the present varicose curtain shows a reflectional symmetry, the vanishing nature of the cross-correlation cannot be interpreted as an indicator of mixing homogeneity at the measurement time ($t^* = 22.9$). This issue will be revisited in a subsequent section on Reynolds shear stresses.

Figure 7(*b*) plots histograms of the variance of the velocity fluctuations and the instantaneous cross-velocity correlation ($u_1' u_2'$). The histograms are computed based on fluctuating velocities in all of the instantaneous realizations prior to taking the ensemble averages. The symmetric nature of the cross-velocity correlation is consistent with the vanishing nature of this correlation observed earlier. In addition, in an area-averaged sense, the streamwise and spanwise velocity variances appear nearly identical.

The dependence of the turbulent velocity statistics on the PIV interrogation window size was investigated by interrogating the PIV images with multiple window sizes. It was found that a 24 × 24 pixel interrogation window captured the statistics better than larger windows. A 32 × 32 pixel interrogation window (corresponding to a resolution of 242 μm at 50 % overlap) underestimated the $\sigma_u$ and $\sigma_v$ statistics by 5–10 % compared to a 24 × 24 pixel window (resolution of 182 μm). The size of the window was observed to have a negligible influence on the mean velocity statistics.

### 3.7. *Mean density and density probability density function*

The mean density profile of the gas curtain before ($t^* = 15.4$) and after ($t^* = 22.9$) reshock are shown in figure 8. The mean densities were calculated as the spanwise average of the ensemble-averaged density field. These profiles were calculated after correcting for small centre-of-mass variations between the shots. The uneven pattern of the mean density profile before reshock is a direct consequence of the mass distribution induced by the growing RM instability. The disorderly mixing induced by the reshock reduces these uneven variations and results in a more evenly distributed density profile. The peak density occurs on the downstream side of the curtain after

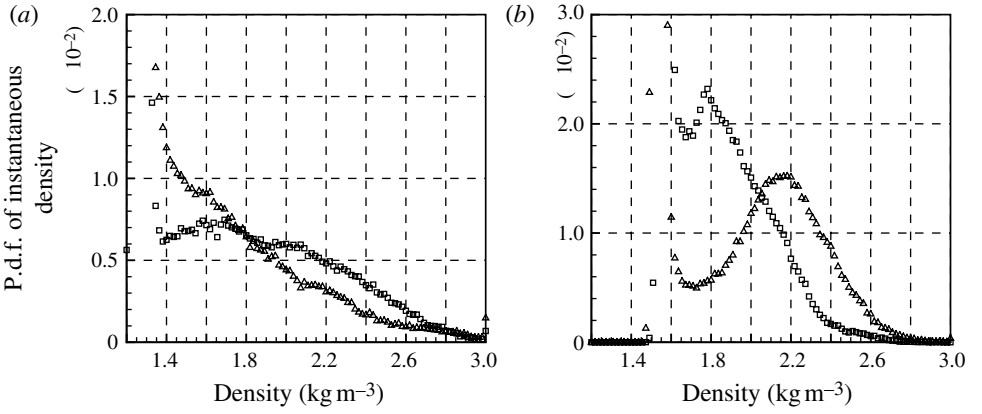


FIGURE 9. P.d.f. of the instantaneous density field for (*a*) pre-reshock case at $t^* = 15.4$ and (*b*) post-reshock case at $t^* = 22.9$ on the upstream (□) and downstream (△) sides of the centre of mass. The p.d.f. is calculated over an area that spans $1.44\lambda$ in the streamwise direction and $2.88\lambda$ in the spanwise direction as measured from the centre of mass of the layer. Upstream and downstream directions are with reference to the direction of the first shock.

reshock. The gradient on the downstream side is also steeper than on the upstream side, resulting in a small offset between the location of the peak density and the centre of mass of the fluid layer. The higher mean density after reshock is consistent with the presence of a compressive shock.

The differences between the mixing that occurs on the upstream and downstream sides of the centre of mass of the curtain are investigated by plotting the probability density functions (p.d.f.) of the absolute density on either side of the centre of mass, as shown in figure 9. Both before and after reshock, the asymmetry of the density distributions on either side of the centre of mass imply that the density gradients carry an imprint of the direction of the shock wave.

At $t^* = 15.4$ (before reshock), a larger fraction of the heavier-density clumps occur in the upstream side and are located closer to the centre of mass when compared to the lighter clumps. On the other hand, after reshock, a larger fraction of the heavier clumps occur in the downstream side and are located further from the centre of mass compared to the lighter material. After reshock, a peak in the p.d.f. occurs at a density of $\sim 2.15$ kg m$^{-3}$ on the downstream side. This peak is absent in the pre-reshocked density p.d.f. and is created by the rapid mixing between the air and $SF_6$ after reshock.

### 3.8. *Density self-correlation: dependence on the method of averaging*

Several types of averages can be constructed from an ensemble of realizations, including spatial averages out of single realizations (Cook *et al.* 2004) and true ensemble averages. Since the computationally intensive nature of high-resolution numerical simulations often allows only the calculation of averages from a single realization, an examination of the differences between spatial averages and ensemble averages becomes critical, especially when ensemble-averaged experimental data are used to validate simulations. Here, we examine the differences observed in the density self-correlation (DSC) profiles between spatially averaged statistics from a single realization, and ensemble averages calculated from multiple realizations of the instantaneous density field. The DSC (denoted by $b$) is an indicator of the state of fluid mixing, and occurs unclosed in variable-density turbulent flows as a multiplier in

the production term of the mass flux equation. Thus, the DSC is an important quantity that mediates turbulent mass flux and material mixing in variable-density flows. The DSC can be defined using both the mean density and the fluctuating density fields as follows (Besnard *et al.* 1992):

$$b = \overline{-\rho'\left(\frac{1}{\rho}\right)'} = \overline{\rho}\,\overline{\left(\frac{1}{\rho}\right)} - 1. \tag{3.1}$$

Note that the DSC is non-negative by definition and can be calculated using only mean density and mean specific volume measurements in a turbulent flow field. Also, the definition of DSC does not involve velocities and is therefore a convenient quantity to measure experimentally using only density measurement diagnostics (e.g. PLIF).

In the present work, the DSCs from single realizations are calculated using the mean density and mean specific volume averages in the spanwise direction. The pointwise DSC field is then averaged in the spanwise direction for convergence. The following equations represent the averaging process used for computing the DSC from single realizations (where overbars represent spatial averages, and subscripts $x$ and $y$ denote averaging in the streamwise and spanwise directions, respectively):

$$\overline{\rho}(x) = \overline{\rho(x,y)}^{y}, \tag{3.2}$$

$$\rho'(x,y) = \rho(x,y) - \overline{\rho}(x), \tag{3.3}$$

$$b(x) = \overline{-\rho'(x,y)\left(\frac{1}{\rho}\right)'}^{y}. \tag{3.4}$$

The ensemble-averaged DSC profiles are calculated using the mean density and specific volume ensemble averages. The pointwise DSC fields are then averaged in the spanwise direction as shown below (where $\langle\cdots\rangle$ denotes an ensemble average, and subscript $i$ denotes the $i$th instantaneous realization):

$$\overline{\rho}(x,y) = \langle \rho_i(x,y)\rangle, \tag{3.5}$$

$$\rho_i'(x,y) = \rho_i(x,y) - \overline{\rho}(x), \tag{3.6}$$

$$b(x,y) = -\left\langle \rho_i'(x,y)\left(\frac{1}{\rho_i}\right)'\right\rangle, \tag{3.7}$$

$$b(x) = \overline{b(x,y)}^{y}. \tag{3.8}$$

Figure 10 shows the DSC variation calculated using both the methods before and after reshock. Significant differences between the ensemble-averaged and single realization statistics are observed. In general, single realizations yield larger values when compared to ensemble statistics. This is particularly true near the edges, which are sensitive to initial conditions. Here, the presence of high-density material projectiles (Zabusky 1999) that are sensitive to small variations in the experimental conditions result in large contributions to the fluctuating quantities and affect the DSC. Throughout the fluid layer, the DSC varies by a factor of 2–3 between the two methods (single realization and ensemble averaging).

### 3.9. *Turbulent mass flux estimates*

The turbulent mass flux velocities ($a_i$) through the fluid layer are given by

$$a_i = \overline{\rho' u_i'}/\overline{\rho}. \tag{3.9}$$

The mass fluxes due to turbulent fluctuations are calculated directly in the present flow from the simultaneous PIV–PLIF measurements. In order to obtain convergent

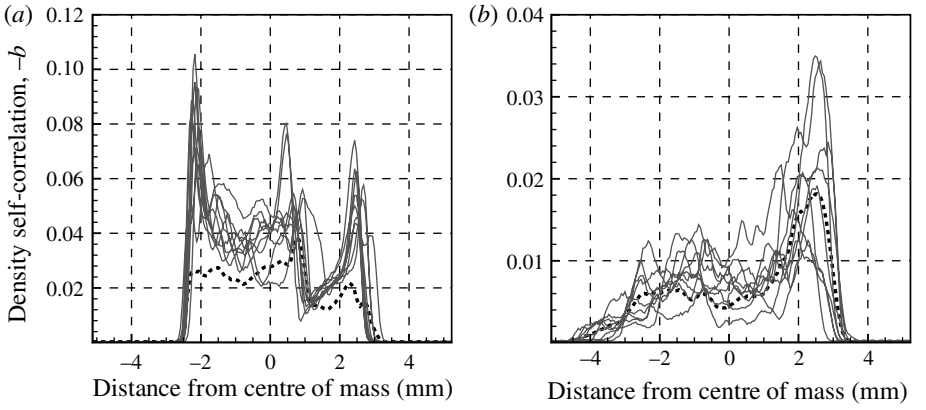


FIGURE 10. Density self-correlation measurements calculated from single realizations (solid) and from ensemble averages (dashed) showing the dependence of DSC on the method of averaging (*a*) before reshock ($t^* = 15.4$) and (*b*) after reshock ($t^* = 22.9$).

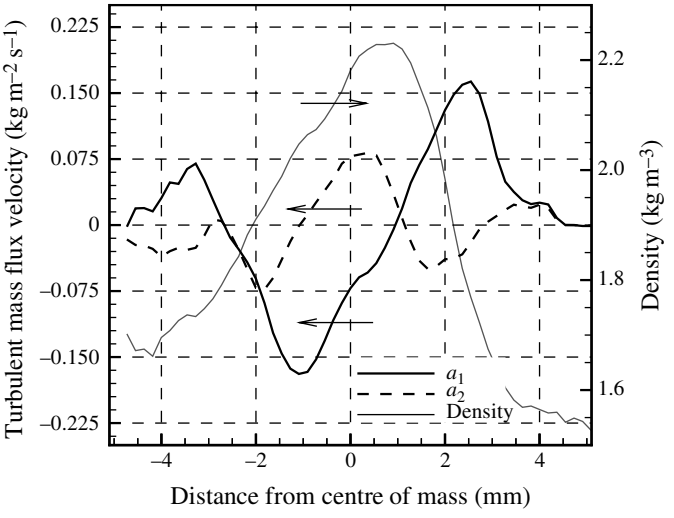


FIGURE 11. Turbulent mass flux and density variations across the fluid layer after reshock ($t^* = 22.9$). The zero-crossing location of the streamwise turbulent mass flux coincides with the peak in the density profile.

statistics, ensemble averages followed by spanwise averages have been calculated on the measured instantaneous fields. The variation of the turbulent mass flux in the fluid layer after reshock, along with the density profile variation in the streamwise direction, is shown in figure 11. The turbulent mass flux plots shown here have been smoothed with a five-point moving average filter prior to plotting.

The streamwise turbulent mass flux ($\overline{\rho' u_1'}$) is generally negative in the upstream direction (with respect to the first shock) and positive in the downstream direction, with the zero crossing occurring at a streamwise location coincident with the density peak. This behaviour is closely related to the variation of the mean density profile and can be explained using an argument similar to that used to determine the sign of the Reynolds shear stress term in incompressible, single-fluid turbulent flows. Upstream

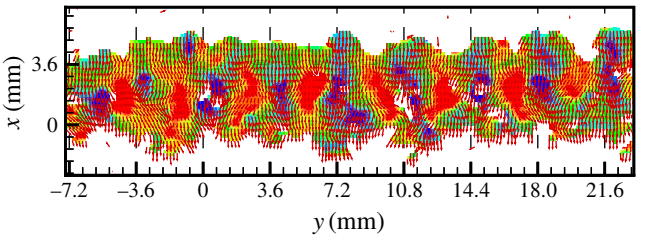


FIGURE 12. Instantaneous streamwise velocity contours superimposed on the velocity vector field to show the presence of initial condition imprints after reshock at $t^* = 22.9$. Red and blue represent high and low streamwise velocity regions, respectively.

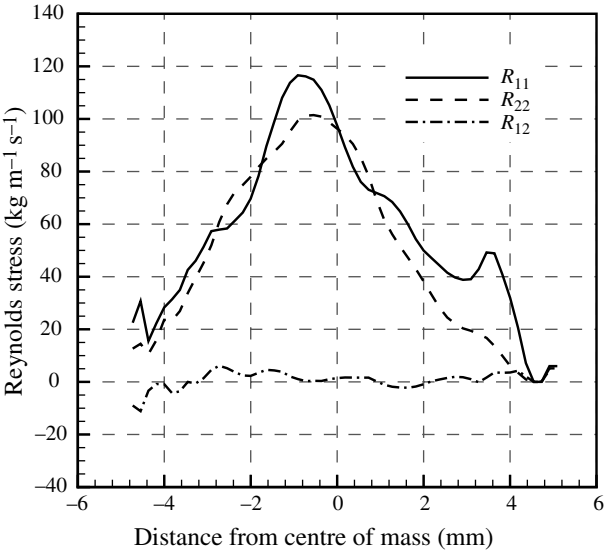


FIGURE 13. Streamwise variation of the Reynolds stresses across the fluid layer after reshock ($t^* = 22.9$).

of the centreline, a fluid parcel subjected to positive streamwise velocity fluctuation is transported to a region of higher density, causing a negative $\rho' u_1'$ correlation. Downstream of the centreline, a positive velocity fluctuation causes the transport of heavier fluid into a lighter fluid region (i.e. positive density fluctuation), resulting in a positive $\rho' u_1'$ correlation. Thus, the sign of $\rho' u_1'$ is determined by the gradient of the density field.

In a fully mixed state, where spanwise inhomogeneities are absent, the spanwise turbulent mass flux ($\overline{\rho' u_2'}$) should vanish by symmetry. However, the spanwise turbulent mass flux in the present case is measured to be non-zero, giving rise to the possibility that the flow might not be fully mixed at the observation time. Although this is not readily seen in the density fields, a strong spanwise variation in the flow field is observed in a plot of the streamwise velocity contours (figure 12). The spanwise spacing between the contour peaks is nearly 3.6 mm, corresponding to the initial wavelength of the instability. Thus, the mixing zone has not yet attained a state of spanwise homogeneity in the present case at $t^* = 22.9$.

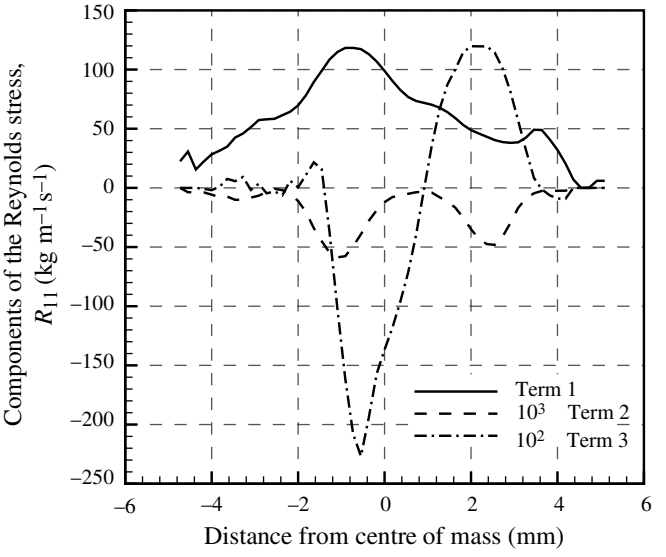


FIGURE 14. Various components of the Reynolds stress term, $R_{11}$, after reshock ($t^* = 22.9$).

The generalized mass-weighted Reynolds stresses, $R_{ij} = \overline{\rho u_i'' u_j''}$, where $u_i''$ is the Favre velocity fluctuation, determine the turbulent transport of momentum in variable-density flows. In the present case, three of the six independent components of this tensor can be directly measured. Figure 13 shows the streamwise variation of the Reynolds stresses $R_{11}$, $R_{22}$ and $R_{12}$. As expected from the values of the turbulent fluctuations, the self-correlation terms $R_{11}$ and $R_{22}$ are similar in magnitude, and the cross-correlation term $R_{12}$ is significantly smaller. More interestingly, the Reynolds stresses can also be written as

$$R_{ij} = \underbrace{\overline{\rho} \overline{u_i' u_j'}}_{\text{term 1}} - \underbrace{\overline{\rho} a_i a_j}_{\text{term 2}} + \underbrace{\overline{\rho' u_i' u_j'}}_{\text{term 3}} \tag{3.10}$$

The various terms in this equation are shown in figure 14. Although shown only for $R_{11}$, the trends are similar for $R_{22}$ and $R_{12}$, and the ensuing discussion pertains to these terms also. It is clear that, at the measurement location, the Reynolds stresses are dominated by the $\overline{\rho}\, \overline{u_i' u_j'}$ term (term 1), with the other two terms being substantially smaller. In particular, the mass flux term (term 2) is $\sim$10 times smaller than the triple correlation term (term 3), which, in turn, is $\sim$100 times smaller than the dominant term (term 1). Thus, from a modelling perspective, the mean density–velocity correlation terms are the most dominant terms that contribute to the Reynolds stresses.

## 4. Summary

The statistics of turbulent mixing in an RM unstable, variable-density fluid layer were measured using high-resolution, simultaneous velocity–density diagnostics (PIV–PLIF) in a varicose fluid layer after reshock. Such detailed, multi-point statistical measurements of the turbulent density–velocity fields, performed in RM flows for the first time, offer several new insights into RM material mixing in the turbulent mixing regime.

At low Mach numbers ($Ma = 1.21$) and moderate Atwood numbers ($At = 0.67$), we observe that a single shock does not induce a transition to turbulence within the times observed ($t^* = tU/\lambda < 23.4$). However, an immediate transition to a turbulent mixing state accompanied by strong mixing occurs within $t^* = 2.9$ of impact by a reshock wave at $t^* = 17.2$. Unlike the singly shocked case, where the mixing is driven only by the vortex-induced fluid motion generated by a stable arrangement of vortices, after reshock, the mixing appears more chaotic and is associated with clear vortical motions inside the mixing layer, resulting in a faster transition to a turbulent state. These motions are associated with strong streamwise and spanwise velocity fluctuations (up to 30 % of the mean convection velocity of the fluid layer) at $t^* = 22.9$. These fluctuation magnitudes were larger than the measurements at an earlier time (Balakumar *et al.* 2008), indicating turbulence production long after shock passage, possibly due to variable-density effects. The r.m.s. streamwise and spanwise velocity fluctuations were measured to be approximately equal (within experimental errors) across the fluid layer. One implication of this observation is the possibility that the three-dimensional mixing after reshock acts to reduce any shock-induced anisotropy.

Mean density profiles across the curtain showed asymmetric distributions about the centreline after reshock. Despite the symmetry of the initial conditions, the downstream side of the fluid layer carried larger density gradients compared to the upstream side. This observation is consistent with a small offset between the location of the density peak and the centre of mass. The p.d.f.s of the instantaneous density fields after reshock showed a peak at a density of 2.15 kg $m^{-3}$, presumably created by the rapid mixing between the light and heavy fluids to create an intermediate mixed fluid.

A comparison of the DSC, calculated both from instantaneous spanwise averages and from ensemble averages, showed significant differences between the two methods (up to ±55 % variation near the peak). Computations that often rely on single realizations must take this observation into consideration prior to a comparison with experimental data. The instantaneous spanwise-averaged statistics of the DSC, obtained from single realizations of the experiment, were observed to be within a factor of 2–3 of the ensemble statistics. This provides a bound for comparison of simulations to experiments.

The measured streamwise turbulent mass flux ($\overline{\rho' u_1'}$) showed opposite signs on either side of the density peak within the curtain. This behaviour was explained by examining the events that generate turbulent mass fluxes inside RM curtains. Considering the portion of the fluid layer on the upstream side of the density peak, a positive streamwise velocity fluctuation (i.e. a velocity surplus along the downstream direction with respect to the first shock) transports lower-density fluid into the measurement point. Conversely, a negative velocity fluctuation transports higher-density fluid present closer to the density peak to the measurement location. Hence, a strong negative correlation between the density and velocity fluctuations is established, resulting in a negative turbulent mass flux. Based on this observation, the turbulent transport of material within RM curtains depends on the gradient of the density. At the measurement location ($t^* = 22.9$), a lack of homogeneous mixing (and consequently evidence for the presence of an imprint of the initial conditions) is observed in the spanwise periodicity of the streamwise velocity contours, consistent with the non-zero value of the spanwise turbulent mass flux.

Using two-dimensional velocity–density measurements, three of the six independent components of the general Reynolds stress tensor ($\overline{\rho u_i'' u_j''}$) were directly measured. The self-correlation terms ($R_{11}$ and $R_{22}$) were similar in magnitude, while the cross-correlation term ($R_{12}$) was observed to be much smaller. When the Reynolds stress term is written as $R_{ij} = \overline{\rho}\,\overline{u_i' u_j'} - \overline{\rho} a_i a_j + \overline{\rho' u_i' u_j'}$, in all the three measured terms $(R_{11}, R_{22}, R_{12})$ the Reynolds stresses are dominated by the $\overline{\rho}\,\overline{u_i' u_j'}$ term, with the remaining terms being at least one order of magnitude smaller.

## Acknowledgements

The authors gratefully acknowledge the support of the US Department of Energy, and the valuable comments of the reviewers.

## REFERENCES

ABARZHI, S. I. 2010 On fundamentals of Rayleigh–Taylor turbulent mixing. *Europhys. Lett.* **91**, 35001.

ADRIAN, R. J. & WESTERWEEL, J. 2010 *Particle Image Velocimetry*. Cambridge University Press.

AGLITSKIY, Y., VELIKOVICH, A. L., KARASIK, M., METZLER, N., ZALESAK, S. T., SCHMITT, A. J., PHILIPS, L., GARDNER, J. H., SERLIN, V., WEAVER, J. L. & OBENSCHAIN, S. P. 2010 Basic hydrodynamics of Richtmyer–Meshkov-type growth and oscillations in the inertial confinement fusion-relevant conditions. *Phil. Trans. R. Soc.* A **368**, 1739–1768.

ARNETT, W. D., BAHCALL, J. N., KIRSHNER, R. P. & WOOSLEY, S. E. 1987 Supernova 1987a. *Annu. Rev. Astron. Astrophys.* **27**, 629–700.

BALAKUMAR, B. J., ORLICZ, G. C., TOMKINS, C. D. & PRESTRIDGE, K. P. 2008 Simultaneous particle-image velocimetry–planar laser-induced fluorescence measurements of Richtmyer–Meshkov instability growth in a gas curtain with and without reshock. *Phys. Fluids* **20** (12), 124103.

BALASUBRAMANIAN, S., ORLICZ, G., PRESTRIDGE, K. P. & BALAKUMAR, B. J. 2011 Influence of initial conditions on turbulent mixing in shock driven Richtmyer–Meshkov flows, *AIAA Paper* 2011-3710.

BANERJEE, A., GORE, R. A. & ANDREWS, M. J. 2010*a* Development and validation of a turbulent-mix model for variable density and compressible flows. *Phys. Rev.* E **82**, 046309.

BANERJEE, A., KRAFT, W. N. & ANDREWS, M. J. 2010*b* Detailed measurements of a statistically steady Rayleigh–Taylor mixing layer from small to high Atwood numbers. *J. Fluid Mech.* **659**, 127–190.

BENEDICT, L. H. & GOULD, R. D. 1996 Towards better uncertainty estimates for turbulence statistics. *Exp. Fluids* **22**, 130–136.

BESNARD, D., HARLOW, F. H., RAUENZAHN, R. M. & ZEMACH, C. 1992 Turbulence transport equations for variable-density turbulence and their relationship to two-field models. *Tech. Rep.* LA-12303-MS. Los Alamos National Laboratory.

BEVINGTON, P. R. 1969 *Data Reduction and Error Analysis for the Physical Sciences*. McGraw-Hill.

CHASSAING, P., ANTONIA, R. A., ANSELMET, F., JOLY, L. & SARKAR, S. 2002 *Variable Density Fluid Turbulence*. Kluwer Academic.

COOK, A. W., CABOT, W. & MILLER, P. L. 2004 The mixing transition in Rayleigh–Taylor instability. *J. Fluid Mech.* **511**, 333–363.

DIMOTAKIS, P. E. 2005 Turbulent mixing. *Annu. Rev. Fluid Mech.* **37**, 329–356.

GOWARDHAN, A., BALASUBRAMANIAN, S., GRINSTEIN, F. F., PRESTRIDGE, K. & RISTORCELLI, R. 2011 Analysis of computational and laboratory shocked gas-curtain experiments. *AIAA Paper* 2011-3040.

GOWARDHAN, A. & GRINSTEIN, F. 2010 Simulation of material mixing in shocked and reshocked gas-curtain experiments. In *Bulletin of the American Physical Society, Division of Fluid Dynamics Meeting, 21–23 November 2010, Long Beach, CA*. APS.

GOWARDHAN, A. A., GRINSTEIN, F. F. & WACHTOR, A. J. 2010 Three dimensional simulations of Richtmyer–Meshkov instabilities in shock tube experiments. *AIAA Paper* 2010-1075.

HILL, D. J., PANTANO, C. & PULLIN, D. I. 2006 Large-eddy simulation and multiscale modelling of a Richtmyer–Meshkov instability with reshock. *J. Fluid Mech.* **557**, 29–61.

HINZE, J. O. 1959 *Turbulence*. McGraw-Hill.

JACOBS, J. W., JENKINS, D. G., KLEIN, D. L. & BENJAMIN, R. F. 1995 Nonlinear growth of the shock-accelerated instability of a thin fluid layer. *J. Fluid Mech.* **295**, 23–42.

JOURDAN, G., SCHWAEDERLE, L., HOUAS, L., HAAS, J.-F., ALESHIN, A. N., SERGEEV, S. V. & ZAYTSEV, S. G. 2001 Hot-wire method for measurements of turbulent mixing induced by Richtmyer–Meshkov instability in shock tube. *Shock Waves* **11**, 189–197.

VON KÁRMÁN, T. 1938 Some remarks on the statistical theory of turbulence. In *Proceedings of the Fifth International Congress for Applied Mechanics, 12–16 September 1938, Cambridge, MA* (ed. J. P. den Hartog & H. Peters). John Wiley and Sons Inc., New York, NY (USA) & Chapman and Hall Ltd, London (UK), 1939.

LATINI, M., SCHILLING, O. & DON, W. S. 2007 High-resolution simulations and modelling of reshocked single-mode Richtmyer–Meshkov instability: comparison to experimental data and to amplitude growth model predictions. *Phys. Fluids* **19**, 024104.

LIVESCU, D. & RISTORCELLI, J. R. 2007 Buoyancy-driven variable-density turbulence. *J. Fluid Mech.* **591**, 43–71.

LIVESCU, D. & RISTORCELLI, J. R. 2008 Variable-density mixing in buoyancy-driven turbulence. *J. Fluid Mech.* **605**, 145–180.

LIVESCU, D., RISTORCELLI, J. R., GORE, R. A., DEAN, S. H., CABOT, W. H. & COOK, A. W. 2009 High-Reynolds number Rayleigh–Taylor turbulence. *J. Turbul.* **10** (13), 1–32.

MARIANI, C., JOURDAN, G., HOUAS, L. & SCHWAEDERLE, L. 2009 Hot wire, laser Doppler measurements and visualization of shock induced turbulent mixing zones. *Shock Waves* **18**, 1181–1186.

MARUSIC, I. 2001 On the role of large-scale structures in wall turbulence. *Phys. Fluids* **13**, 735.

MAUREL, A., ERN, P., ZIELINSKA, B. J. A. & WESFREID, J. E. 1996 Experimental study of self-sustained oscillations in a confined jet. *Phys. Rev.* E **54**, 3643–3651.

NISHIHARA, K., WOUCHUK, J. G., MATSUOKA, C., ISHIZAKI, R. & ZHAKHOVSKY, V. V. 2010 Richtmyer–Meshkov instability: theory of linear and nonlinear evolution. *Phil. Trans. R. Soc.* A **368**, 1769–1807.

ORLICZ, G. C., BALAKUMAR, B. J., TOMKINS, C. D. & PRESTRIDGE, K. P. 2009 A Mach number study of the Richtmyer–Meshkov instability in a varicose, heavy-gas curtain. *Phys. Fluids* **21**, 064102.

ORLOV, S. S., ABARZHI, S., OH, S. B., BARBASTATHIS, G. & SREENIVASAN, K. R. 2010 High-performance holographic technologies for fluid-dynamics experiments. *Phil. Trans. R. Soc.* A **368**, 1705–1737.

POGGI, F., THOREMBEY, M. H. & RODRIGUEZ, G. 1998 Velocity measurements in turbulent gaseous mixtures induced by Richtmyer–Meshkov instability. *Phys. Fluids* **10** (11), 2698–2700.

RICHTMYER, R. D. 1960 Taylor instability in shock acceleration of compressible fluids. *Commun. Pure Appl. Maths* **13**, 297–319.

RISTORCELLI, J. R. & CLARK, T. T. 2004 Rayleigh–Taylor turbulence: self-similar analysis and direct numerical simulations. *J. Fluid Mech.* **507**, 213–253.

ROBEY, H. F., ZHOU, Y., BUCKINGHAM, A. C., KEITER, P., REMINGTON, B. A. & DRAKE, R. P. 2003 The time scale for the transition to turbulence in a high Reynolds number, accelerated flow. *Phys. Plasmas* **10** (3), 614–622.

RYUTOV, D., DRAKE, R. P., KANE, J., LIANG, E., REMINGTON, B. A. & WOOD-VASEY, W. M. 1999 Similarity criteria for the laboratory simulation of supernova hydrodynamics. *Astrophys. J.* **518** (2), 821–832.

SOLOFF, S. M., ADRIAN, R. J. & LIU, Z. C. 1997 Distortion compensation for generalized stereoscopic particle image velocimetry. *Meas. Sci. Technol.* **8** (12), 1441–1454.

THORNBER, B., DRIKAKIS, D., YOUNGS, D. L. & WILLIAMS, R. J. R. 2010 The influence of initial conditions on turbulent mixing due to Richtmyer–Meshkov instability. *J. Fluid Mech.* **654**, 99–139.

TOMKINS, C., KUMAR, S., ORLICZ, G. & PRESTRIDGE, K. 2008 An experimental investigation of mixing mechanisms in shock-accelerated flow. *J. Fluid Mech.* **611**, 131–150.

VELIKOVICH, A. L., DAHLBURG, J. P., SCHMITT, A. J., GARDNER, J. H., PHILLIPS, L., COCHRAN, F. L., CHONG, Y. K., DIMONTE, G. & METZLER, N. 2000 Richtmyer–Meshkov-like instabilities and early-time perturbation growth in laser targets and Z-pinch loads. *Phys. Plasmas* **7** (5), 1662–1671.

WARHAFT, Z. 2000 Passive scalars in turbulent flows. *Annu. Rev. Fluid Mech.* **32**, 203–240.

YANG, J., KUBOTA, T. & ZUKOSKI, E. E. 1993 Applications of shock-induced mixing to supersonic combustion. *AIAA J.* **31** (5), 854–862.

ZABUSKY, N. J. 1999 Vortex paradigm for accelerated inhomogeneous flows: visiometrics for the Rayleigh–Taylor and Richtmyer–Meshkov environments. *Annu. Rev. Fluid Mech.* **31**, 495–536.

ZOLDI-SOOD, C., GORE, R., BALAKUMAR, B. J., ORLICZ, G., RANJAN, D., TOMKINS, C. & PRESTRIDGE, K. 2008 Simulations of a reshocked varicose gas curtain. In *Bulletin of the American Physical Society, Division of Fluid Dynamics Meeting, 23–25 November 2008, San Antonio, TX*. APS.